

Multi Satellite Comparisons of the Radiation Belt Response to the GEM magnetic storms

K. L. McAdams, G. D. Reeves, & R. Friedel

Los Alamos National Laboratory, Los Alamos, New Mexico

Short title: GEM STORM COMPARISONS

Abstract.

1. Introduction

The population of relativistic electrons in the Earth's outer radiation belt varies dramatically with magnetic activity. As we increase our reliance on satellite technology, the response of the radiation belt electrons to magnetospheric conditions is of more than academic interest because elevated relativistic electron fluxes can interfere with satellite operations. Relativistic electron flux increases in the radiation belts occur during disturbed solar wind conditions such as magnetic cloud events and coronal mass ejections (CME's) [REEVES,???].

Although the relationship between relativistic electron fluxes and magnetic storms has been known for many years [*Paulikas and Blake, 1979*], it is not clear by what mechanism magnetic storms accelerate the relativistic electron population. Several studies have examined the temporal development at different L-shells of particular storms [*Reeves et al., unknown; Selesnick and Blake, 1999*], however, the variation of the temporal profile during different storms has not been examined. The location of the peak in the phase space density (PSD) of the electrons is still a point of debate and indeed may vary from storm to storm [*Selesnick and Blake, 1999; Green et al., 1999*]. Few observations of the peak PSD have been made, primarily because phase space density measurements using adiabatic coordinates are difficult to calculate, as they require good energy and pitch angle resolution as well as reliable magnetic field measurements and models. Unfortunately, most magnetic field models are not valid during storm-time disturbances—the precise time interval in which electron enhancements occur. Another

piece of the puzzle which is key to several acceleration mechanisms [*Li et al.*, 1999], is whether there is a population of “seed” electrons in the outer magnetosphere and where that population might be located.

There are several competing and intertwined theories to explain how the acceleration of the relativistic electrons occurs in magnetic storms. There is evidence that when there is a large shock related compression of the magnetopause, the production of a large induction electric field can rapidly accelerate an existing seed electron population which subsequently move to lower L-shells to preserve the third adiabatic invariant [*Li et al.*, 1998]. In most storms, however, there is no large compressional shock and other mechanisms must be invoked. *Nishida* [1976] and *Fujimoto and Nishida* [1990] proposed a magnetic pumping/recirculation model, in which diffusive processes combine to slowly accelerate electrons through successive cycles, moving particles in to lower L-shells and back out to higher ones. *Liu et al.* [1999] modified this theory by incorporating a ULF wave rather than pitch angle diffusion to scatter the electrons to speed up the cycle time resulting in a timescale of electron heating consistent with observations of the electron response to storms. Others have incorporated ULF wave interactions in several ways to directly heat the electrons to high energies (ie, *Hudson et al.* [1999]; *Elkington et al.* [1999]). Whistler mode interactions with the electrons near the plasmapause are also considered by Thorne (BIB).

In order to understand the response of the magnetosphere, including the radiation belts, to magnetic storm conditions the GEM community has identified three magnetic storms for in-depth study and comparison. These storms include May 15, 1997;

September 25, 1998; and October 20, 1998; we have included January 10, 1997, as it is a well studied example of a magnetic storm accompanied by a compressional shock. We present observations of all four storms in order to constrain the theoretical understanding of the acceleration of radiation belt electrons.

In this paper we present a compilation of observations of the four GEM storms from instruments on 10 separate spacecraft in order to place observational constraints on theoretical models of the radiation belt electron acceleration. After comparison of the storms, we determine the general characteristics of the electron storm-time response in the radiation belts ($2 < L < 7$). We also identify characteristics which are particular to an individual storm and propose explanations for the differences between the storms.

2. Data Synthesis Techniques

2.1. Motivation

Data from a single spacecraft has the well known drawback that single point measurements cannot differentiate spatial and temporal variations. Synthesizing data from many spacecraft into a single data set, providing both space and time coverage, allows a more complete view of radiation belt dynamics. Instruments on different satellites vary widely from high energy resolution and pitch-angle resolution detectors designed to explore the radiation belts to single-energy-channel detectors built primarily to understand the radiation dose at the satellite. By combining data sets from various instrument platforms, we can often “bootstrap” the data from a low-resolution

instrument by using pitch angle or magnetic field measurements from nearby spacecraft to make informed assumptions applicable at other satellites.

For this study, we have included data from ten satellites, each with electron instruments that detect electrons greater than 1 MeV. The additional instruments on each payload vary widely. The POLAR satellite [*Blake et al.*, 1995] has the most complete instrument package in this set of satellites, including magnetometers and electron detectors sensitive to a large range of energies and different pitch angles. POLAR has a long orbital period (18 hours) and hence has relatively low time coverage through the radiation belts. SAMPEX has a short orbital period and very good time coverage of the radiation belts, but has limited spectral information and no magnetometer [*Baker et al.*, 1993]. The HEO satellite has a single integral channel which detects electrons greater than 1.5 MeV [*Blake et al.*, 1997]. The GPS satellites (NS 24 and NS 33) have an orbit such that they are near the equator at an L-shell of 4.2, and can obtain reasonable spectral information [*Feldman et al.*, 1985]. At geosynchronous altitude, the Los Alamos National Laboratory (LANL) satellites 1994-084, 1991-080, and 1990-095 provide good spectral information at near equatorial latitudes [*Reeves et al.*, 1997]. The GOES satellites, also in geosynchronous orbit, provide limited spectral information, but carry magnetometers [*Space-Systems-Loral*, 1996]. Table 1 summarizes the instrumentation of each satellite which is included in this study.

By simultaneously including data from satellites at the same nominal L-shell but different magnetic local times (MLT), we can show either local time differences in the flux evolution or, as is done here, average over these differences and show a more general

picture of the global electron flux evolution. Although there is generally a latitudinal invariance in the fluxes along a single L-shell, during highly disturbed times there is a tendency to see the electron fluxes increase first at high altitudes (near the equator) rather than at low altitudes (nearer the poles) on the same field line. [Blake, personal communication, 2000]

2.2. Method

Combining ten single-satellite data sets into a coherent picture of the radiation belts requires careful data manipulation. Differences in the energy and pitch angle ranges must be accounted for as well as any latitudinal variation. Compounding this problem, we often do not know the pitch angle distribution at each satellite, nor do we have spectral information from each satellite. Therefore, we have made several—admittedly simplistic—assumptions: 1) The pitch angle distribution is isotropic throughout the evolution of the storm. This is almost certainly not valid for some of the time, as NEED NAME HERE have shown that the distribution tends to form butterfly or pancake distributions. However, isotropy is a commonly invoked assumption and is likely to be accurate during the recovery of the storm. 2) The spectral shape does not change drastically at energies greater than 1 MeV. This allows us to compare flux from a 1 MeV channel to flux from a 2.0 MeV channel and use a constant normalization factor throughout the storm. This assumption is fairly good at lower L-shells, as we show later in the paper (see Section 4.2).

We normalize the flux levels at each satellite to account for the energy range and

pitch angle differences. First, we normalize the geosynchronous satellites (LANL & GOES) to each other by fitting the data during the rise and fall of the fluxes after the main phase of the storm to a parabola using only the data near magnetic local noon for each satellite. Fluxes are taken at local noon to minimize fluctuations on the night-side due to substorm activity. By means of a multiplicative factor, we adjust the apex of each parabola so that all the parabolas have the same apex. This factor is the normalization factor for the geosynchronous satellites, less than a factor of 2 for the five geosynchronous satellites.

We standardize the magnetic coordinates for each satellite to a single magnetic field model. We use the Olson-Pfitzer model [*Olson and Pfitzer, 1977*] for simplicity and calculate the magnetic coordinates of each satellite. Assuming isotropic fluxes, we map the electron fluxes to the equatorial plane using a simple B_{sat}/B_{eq} multiplicative factor where B_{eq} is the equatorial magnetic field and B_{sat} is the magnetic field at the satellite.

We tie the non-geosynchronous satellite fluxes to the flux measured by POLAR at $L = 4.5 \pm 0.25$ because POLAR has a well calibrated electron detector (CEPPAD). This adjustment is done by dividing the storm period into individual 24-hour periods. The average flux at $L = 4.5 \pm 0.25$ for each satellite is then compared to the average POLAR flux for the n^{th} period and a multiplicative factor (β_n) is obtained. The mean β for each satellite is then the normalization factor for each storm at all L-shells. This factor incorporates differences in energy ranges, pitch angle coverage and background levels.

No attempt to match the geosynchronous fluxes to the POLAR fluxes is made at $L = 6.6$ because the POLAR count rates are too low at this distance to be trustworthy.

However, the synthesis plots in Figure 2 show that the geosynchronous satellite fluxes match very well to the normalized fluxes at nearby L-shells.

3. GEM Storms

The GEM magnetic storms were chosen to represent the spectrum of storm-time conditions in the magnetosphere. Figure 1 shows the magnetospheric and solar wind conditions throughout the four storms. The first panel of each stack shows the Dst index, the lower three panels show solar wind conditions observed by the WIND spacecraft including IMF B_z , solar wind velocity (v_{sw}), and the solar wind ion density (n). The global radiation belt response to these storm conditions is depicted in Figure 2 where results of the data synthesis are shown. These maps of the relativistic electron fluxes as a function of L and time are created by binning the data sets by L and time and ignoring any local time variation in the fluxes. Table 2 summarizes the solar wind and magnetospheric conditions and the relativistic electron response for the four storms.

3.1. January 1997

If only the response of the ring current is considered, the January 10, 1997, (Jan 97) magnetic storm was a fairly small storm. The minimum Dst reached only a fairly modest -80 nT. However, less than a day after the beginning of the storm, the magnetic cloud that caused the storm created a compressional shock which pushed the magnetopause deep into the inner magnetosphere. The solar wind velocity was close to 600 km/s and the density pulse was near 200 cm^{-3} (see Fig. 1a). This resulted in a rapid increase

in the relativistic electron fluxes over a broad range of L-shells. The acceleration of these particles has been discussed by *Li et al.* [1998] who determined that a pre-existing source of particles were energized by the pressure pulse which pushed them into regions of stronger magnetic field (because the first adiabatic invariant was conserved, the particles must gain energy). After the initial flux increase, the particle flux at high L values (near $L = 6.6$) decrease quickly and then gradually peak a few days later as is typical for 1.5 MeV electrons at $L = 6.6$ (Fig. 2a). The initial flux increase at lower L-values ($L = 4.5$) persists throughout the duration of the recovery phase of the storm.

3.2. May 1997

The May 15, 1997, storm (May 97) was a much larger storm and was a fairly “typical” storm in terms of its simple Dst profile and electron response. However, a small magnetic disturbance at the beginning of the month may have contributed to high flux levels observed prior to the storm onset. In this storm, the Dst minimum of -150 nT coincided with a 44 cm^{-3} density pulse in the solar wind and the ramping up of the solar wind velocity (Fig. 1b). The solar wind velocity continued to increase throughout the main phase of the storm to a maximum of 500 km/s.

The response of the relativistic electrons was much stronger than in Jan 97 as is shown in Figure 2b. The fluxes at low L quickly rise to, and then persist at levels much higher than the Jan 97 storm. At higher L-shells the relativistic electron fluxes take several days to peak at slightly higher flux levels than the January storm. *Baker et al.* [1998] discusses the detailed electron response to this storm and concludes that ULF

waves are probably important in the electron acceleration for this event.

3.3. September 1998

The largest and most complex storm in this study is September 25, 1998 (Sept 98). This storm is a compound event with a large storm (Dst minimum = -250 nT) on September 25th and then a secondary Dst dip of -70 nT on October 1 (Fig 1c). In this event, the solar wind velocity peaks sharply at a maximum of 930 km/s while the density pulse is fairly small at 20 cm^{-3} . A second spike in the density occurs coincident with the October 1 Dst drop and is followed by a second peak in solar wind velocity. Before the storm occurs there is a pre-existing high relativistic-electron flux at low L (near $L = 3.5$). Figure 2c shows the structure in the Dst profile reflected in the electron fluxes as they increase after the first main phase and then decrease again after the second onset occurs. The electron fluxes recover after the second decrease, but do not reach the previous levels of intensity.

3.4. October 1998

The October 20, 1998 (Oct 98) storm has an interesting solar wind profile. At the time of the Dst minimum (-140 nT), the IMF magnitude increases sharply and the solar wind density peaks at 66 cm^{-3} , much higher than either May 97 or Sept 98 (Fig. 1d). The solar wind velocity, however, does not peak at the Dst minimum, but continues to rise for a little over two days to a maximum of 675 km/s. Interestingly, although Oct 98 is a smaller storm than Sept 98 by standards of a Dst drop, the pressure associated

with the density pulse (25 nPa) was slightly higher than the pressure pulse in the Sept 98 storm (24 nPa). Kp values peak at 5.67 coincident with the Dst minimum and then continue to remain active for the next ten days whereas the Sept 98 storm had a sharp peak in Kp that tapered off more quickly.

The electron response is different than that of the other storms (See Figure 2d). At $L = 6.6$ the peak in relativistic electron flux is higher than the $L = 6.6$ peak for the Sept 98 storm even though the Sept 98 storm produced much higher flux levels at lower L values (ie L near 4) than the Oct 98 storm. The ratio of fluxes at $L = 4.2$ to fluxes at $L = 6.6$ is 57 for Sept 98 and 15 for Oct 98. The rise in flux intensities at lower L shells was also more gradual than in the other 3 storms in this study. During the other three storms, the $L = 4$ fluxes rise quickly and then plateau, while in Oct 98 they rise with a more quasi-parabolic temporal profile.

4. Evolution of the Storms at Different L-Shells

In all four of the storms, the evolution of the relativistic electron population varies with L-shell. We examined the the flux evolution at several L-shells to determine the radial progression of the relativistic electron acceleration. We present the radial profiles of intensity, spectral shape and phase space density.

4.1. Flux Intensities

Reeves et al. [unknown] showed that for the Jan 97 storm the time profiles of the fluxes at $L = 4.25$ and $L = 6.6$ are very different: the $L = 4.25$ fluxes peak sooner than

the $L = 6.6$ fluxes. Figure 3 shows the relativistic electron fluxes at $L = 4.25 \pm 0.125$ and $L = 6.6 \pm 0.125$ for the four storms. These fluxes are taken from the synthesis data set and the individual satellite fluxes are color-coded. The spread in fluxes which is particularly noticable at $L = 6.6$ is most likely due to latitudinal effects in addition to the limitations of the magnetic field model in calculating the L-shell values. Jan 97 (Fig 3a) and Sept 98 (Fig 3c) are similar to May 97 in their temporal profiles of the electron flux and comments made about the May 97 storm in reference to this aspect can be applied to them. In Figure 3b, the flux profile at $L = 4.25$ is different from the profile at $L = 6.6$. At $L = 4.25$, the fluxes rise quickly and then plateau, while at $L = 6.6$ the fluxes slowly rise in a quasi-parabolic shape to peak after a few days. This profile is consistent with the findings of *Reeves et al.* [unknown]. The behavior of the electrons during the Oct 98 storm is different from the other three storms. Figure 3d shows that while the flux profile at $L = 6.6$ is unchanged from the other storms, the flux behavior at $L = 4.25$ is different. The profile at $L = 4.25$ shows a more gradual peak in the fluxes rather than a sharp rise which plateaus after a few hours.

It is useful here to compare the electron response of Oct 98 to both May 97 and Sept 98. The May 97 and Oct 98 have similar minimum Dst drops, but the Kp index continues to be at active levels longer during the Oct 98 storm. The solar wind velocity during the May 97 storm is lower than during Oct 98. The maximum flux levels at both $L=4.25$ and $L=6.6$ are higher during the Oct 98 storm even with the similar Dst storm profiles. Oct 98 and Sept 98 have similar peak solar wind dynamic pressure levels, but have very different Dst minimums and solar wind velocity profiles. During

Oct 98, the solar wind velocity continues to climb as the storm progresses, rather than peaking at the same time as the Dst minimum as in Sept 98. Predictably, the stronger Dst minimum of the Sept 98 storm leads to stronger flux levels at $L = 4.25$ than in the Oct 98 storm. However, electron fluxes at $L = 6.6$ are stronger during Oct 98, leading us to speculate that the acceleration mechanisms at work during the two storms may be slightly different.

We believe that these different responses at Oct 98 may be related to the differences in the magnetospheric conditions present during the October storm. Rather than peaking sharply at the time of the DST minimum, the solar wind velocity continued to ramp up during the main phase of the Oct 98 storm. Kp values also remained elevated for several days after the initial burst of activity corresponding to the DST drop. Both of these may have contributed to a continued acceleration of the electrons at $L = 4.0$ and may have played a part in increasing the geosynchronous electron flux to levels higher than during the Sept 98 storm. Although our first inclination was that the continued high solar wind velocity was driving a strong convection electric field during the Oct 98 event, the polar cap index (PCI) during Sept 98 was twice as strong as in Oct 98 indicating a stronger convection field during Sept 98. The Kp index continues to show disturbed conditions with fluctuations up to 4.0 for 5-6 days in Oct 98 while for Sept 98 the disturbed Kp conditions lasted only two days. There are indications that the position of the plasmapause (which can be inferred from Kp index) is important in determining the diffusion coefficient which may play a role in the evolution of the “original” spectra. (NEED TO LOOK UP THE SEBASTIAN BOURDARIE PAPER

HERE)

4.2. Spectral Shape

We determine whether the rise of the relativistic fluxes is due to a change in the spectral shape at high energies. To answer this question, we calculate the energy spectra from electron fluxes at a range of energies from near the equator at $L = 4.25$ (GPS), and $L = 6.6$ (LANL). We take only near-equatorial fluxes so that changes in the spectra due to latitudinal variations can be ignored. The energy range for for GPS NS33 is 0.275-2.2 MeV and for the LANL satellites is 0.200-3.2 MeV. We fit the energy spectra to an exponential: $f(E) = C \exp(-E/E_o)$. (Other functional forms were also fit, but the exponential fit is the most appropriate functional form).

Figure 4 shows the evolution of C (“density”) and E_o (“temperature”) at $L = 4.25$ (GPS) and $L = 6.6$ (LANL). In all four storms there is a fast rise in the C parameter at the main phase of the storm and then a slow, steady decrease at both L-shells shown here. At geosynchronous, all four storms show a gradual rise of E_o , or hardening of the spectra, and then a gradual decline after the storm is over. At $L=4.2$ there is a small drop in E_o at the Dst minimum and then a steady rise corresponding to the recovery phase which continues to rise throughout the depicted interval. The second Sept 98 storm is noticable in the dip of E_o at both L shells (Fig 4c).

The evolution of the high energy electron spectrum during the storm is similar across all four storms regardless of magnetospheric conditions. This general response can be used to understand the basic physics of the storm-time response of the electrons

for most (if not all) storms, hence we offer a physical interpretation of the spectral observations. The response at $L = 4.25$ suggests that during the Dst effect the high energy particles are lost quickly and the spectra softens at the same time that the “density” (C) of the population increases. As the storm progresses, the low energy particles are lost at a higher rate and the spectra slowly hardens without noticeable heating of the high energy tail. The losses can be inferred from the continuing decrease in C as the storm recovers. At geosynchronous, the high energy particles are not lost at the Dst minimum and recovery, indeed, both C and E_o increase during the recovery, indicating heating of the high energy electron tail or of an unlikely inflow of high energy particles without a corresponding low energy population. As the storm progresses, C continues to rise until the peak about 2 days after the initial storm onset. The spectra hardens during this time and E_o peaks approximately 4 days after storm onset. For May 97 the peak in E_o is coincident with the peak in the $> 1\text{MeV}$ particle flux at geosynchronous shown in Figure 3b. We believe the hardening of the spectra at geosynchronous may be due to heating of the high energy tail, rather than losses of the lower energy electrons.

4.3. Phase Space Density

In locating the source of the electron acceleration, it is useful to remove the adiabatic effects from the flux observations so that the non-adiabatic variations are identifiable. One way to do this is to look at the phase space density (PSD) in a coordinate system consisting of the three adiabatic invariants. Calculating the PSD in

adiabatic coordinates from the energy fluxes allows us to follow the motion of fluxes with constant adiabatic invariants. If the adiabatic invariants are conserved, then the radial PSD profile should not vary with time. There are several difficulties involved in this calculation, which are addressed in the next paragraph. The three adiabatic invariants of trapped particle motion are μ , J , and Φ which are associated with gyromotion, bounce motion along the field line and the drift motion around the Earth, respectively. The first invariant is

$$\mu = \frac{p^2}{2mB_m} \quad (1)$$

where p is the momentum, m is the electron rest mass, and B_m is the magnetic field at the electron mirror point. The second invariant is defined by

$$J = \oint p_{\parallel} ds \quad (2)$$

The third invariant (Φ) can be replaced with the generalized L^* shell:

$$L^* = 2\pi k_o a \Phi \quad (3)$$

where Φ is the magnetic flux enclosed by an electron drift orbit, k_o is the Earth's dipole magnetic moment, and a is its radius [Roederer, 1970; Schulz and Lanzerotti, 1974]. We will use the simpler McIlwain L [McIlwain, 1966] which is calculated for the a single field line integral rather than the entire drift shell. By making this substitution, we ignore any local time dependence.

As mentioned earlier, a proper calculation of PSD requires both pitch-angle information and a precise knowledge of the magnetic field structure. We have neither.

However, we can restrict the data sets to locations near the magnetic equator and assume the pitch-angle distribution is isotropic, or at least constant throughout the storm. This allows us to treat the fluxes as if their second adiabatic invariant (J) were strictly zero. We treat the magnetic field as if it were accurately determined by the Olson-Pfitzer field model and assume that the third invariant L^* is proportional to L-shell. By assuming that the particles are equatorially mirroring ($W_{\parallel} = E$), we can assume that the first invariant is given by E/B where E is the energy of the particle and B is the magnetic field at the equator.

Thus, using the same spectra calculated above and by assuming that $\mu = E/B$, $J = 0$ and $L^* \propto L$ we can have an estimate of the PSD at the equator such that

$$F(\mu, J, L^* \sim L) \propto \frac{f(E, \alpha, L)}{E} \quad (4)$$

where F is the PSD, f is the energy flux, and E is the energy of the particles. Now we can compare the PSD at different values of μ for each L-shell above. Figure 5 shows the PSD at 4.25 (GPS) and 6 (LANL) for different values of μ .

The response of the fluxes if one looks at the phase space density is similar for all of the four storms. Figures 5 and 6 show the PSD at 4.25(GPS), and 6.6 (LANL) for different values of μ . The range of μ corresponds to an energy range of 100 keV to 1.5 MeV at L= 6.6 and an energy range of 320 keV to 4.8 MeV at L = 4.25. At L = 4.25, after the initial increase at the Dst recovery, the PSD increases with time at values of μ above some threshold value and decreases with time at values of constant μ less than the threshold. That threshold is near $\mu = 500$ MeV/nT for Jan 97 (Fig 5a) and

$500 < \mu < 935$ May 97 (Fig 5b). For Sept 98 (Fig 6a), the transition appears to occur at lower values of μ , near $\mu = 280$ MeV/nT and for Oct 98 the transition is even lower at $\mu = 93$ MeV/nT (Fig 6b). At $L = 6.6$ all four storms have the same quasi-parabolic shape throughout the storm regardless of μ value. As with the energy fluxes, at low values of μ , the PSD values peak quickly at $L=4.25$, a few days later PSD peaks at $L = 6.6$. The profiles of the PSD values at different L-shells are not very similar which implies that the population is not simply diffusing inward. If the electrons were diffusing in from a distant source population, one would expect that the profiles would be similar even if they were offset by a time delay. However, the profiles shown here imply that there is an additional source of acceleration, other than simple radial diffusion.

5. Discussion

We have examined the relativistic electron response to four different storms, including the three GEM storms (May 97, Sept 98, and Oct 98) and Jan 97. Although these four storms have differing solar wind and ring current conditions, there are a few traits in the electron response that are generally applicable. The evolution of the spectral shape of the electrons above 200 keV is different at $L = 4.25$ and $L=6.6$, although it does not vary from storm to storm. We believe that the difference in the spectral shape may be because the hardening of the spectra at $L = 4.25$ is due to a preferential loss of the low energy electrons while the spectral hardening at $L = 6.6$ is due to an actual heating of the high energy tail rather than a loss of the low energy tail. Examining the phase space density evolution for several values of μ at $L = 6.6$

and $L = 4.25$ we found that the behavior is consistent for the four storms we studied. The PSD profiles are different at the two L -shells implying that the energization of the electrons is not due to a simple diffusive process that does not alter the profile of the electron population that is diffusing in. We found that at low μ values the PSD peaks first at $L = 4.25$ while at high μ values PSD peaks first at $L = 6.6$.

We found that the evolution of the 1.5 MeV fluxes at $L = 4.25$ and $L = 6.6$ was similar for the Jan 97, May 97 and Sept 98 storms while Oct 98 seemed to have a different temporal profile. For the first three storms, the flux profiles were different at the different L values, but for Oct 98 the profiles were more similar. For all four storms, at $L = 6.6$ the profiles are quasi-parabolic in time. For the first three storms the profile at $L = 4.25$ is more plateau-like with a fast rise followed by steady flux levels. Oct 98 is unique among this study in that the $L = 4.25$ flux profile is more similar to that at $L = 6.6$ and is more quasi-parabolic than plateau-like. We attribute this difference in the Oct 98 flux responses to the differences in the solar wind profiles and Kp values. We believe that the continued increase of the solar wind velocity may have contributed to continued acceleration of the electrons at $L=4.25$. The continuing high levels of Kp disturbance may also have contributed to the continuing acceleration of these electrons.

We have found several similarities between the four storms which will help to constrain the theoretical explanations for the acceleration of the relativistic electrons in the radiation belt. Any mechanism to explain the electron acceleration will also have to explain the differences in the electron response to the Oct 98 storm conditions.

Figure 1.

Figure 2.

Figure 3.

Figure 4.

Figure 5.

Acknowledgments.

References

- Baker, D. N., G. M. Mason, O. Figueroa, G. Colon, J. Watzin, and R. M. Aleman, An overview of the solar, anomalous, and magnetospheric particle explorer (sampex) mission., *IEEE Transactions on Geoscience and Remote Sensing*, *31*, 531, 1993.
- Baker, D. N., et al., A stron CME-related magnetic cloud interaction with the earth's magnetosphere: ISTP observations of rapid relativistic electron acceleration on May 15, 1997, *Geophys. Res. Lett.*, *25*, 2975, 1998.
- Blake, J. B., D. N. Baker, N. Turner, K. W. Ogilview, and R. P. Lepping, Correlation of changes in the outer-zone relativistic-electron population with upstream solar wind and magnetic field maeasurements., *Geophys. Res. Lett.*, *24*, 927, 1997.
- Blake, J. B., et al., CEPPAD comprehensive energetic particle and pitch angle distribution experiment on POLAR, in *The Global Geospace Mission*, p. 531, Kluwer Academic Publishers, 1995.
- Elkington, S. R., M. K. Hudson, and A. A. Chan, Acceleration of relativistic electrons via drift-resonant interaction with toroidal-mode Pc-5 ULF oscillation, *Geophys. Res. Lett.*, *26*, 1999.
- Feldman, W., W. aiello, D. Drake, and M. Herrin, The bdd ii: An improved electron dosimeter for the golobal positioning system., *Technical Report LA-10453-MS*, Los Alamos National Laboratory, Los Alamos, NM 87545, USA, 1985.
- Fujimoto, M., and A. Nishida, Energization and anisotropzation of energetic electrons in the earth's radiation belt by the recirculation process, *J. Geophys. Res.*, *95*, 4265, 1990.

- Green, J. C., M. G. Kivelson, and J. B. Blake, Adiabatic electron acceleration and transport during the may 15, 1997 storm, *EOS Trans. AGU*, 80, F894, 1999, SM42B-01.
- Hudson, M. K., S. R. Elkington, J. G. Lyon, C. C. Goodrich, and T. J. Rosenberg, Simulation of radiation belt dynamics driven by solar wind variations, in *Sun-Earth Plasma Connections*, edited by J. L. Burch, R. L. Carovillano, and S. K. Antiochos, vol. 109, p. 171, AGU, Washington, D.C., 1999.
- Li, X., M. Temerin, S. Monk, and D. N. Baker, Outer belt electron enhancements by solar-wind-driven radial diffusion, *EOS Trans. AGU*, 80, F894, 1999, SM42B-02.
- Li, X., et al., Energetic electron injections into the inner magnetosphere during the jan. 10-11, 1997 magnetic storm, *Geophys. Res. Lett.*, 25, 2561, 1998.
- Liu, W. W., B. Rostoker, and D. N. Baker, Internal acceleration of relativistic electrons by large-amplitude ULF pulsations, *J. Geophys. Res.*, 104, 17,391, 1999.
- McIlwain, C. E., Coordinates for mapping the distribution of magnetically trapped particles, *J. Geophys. Res.*, 66, 3681, 1966.
- Nishida, A., Outward diffusion of energetic particles from the Jovian radiation belt, *Geophys. Res. Lett.*, 81, 1771, 1976.
- Olson, W. P., and K. A. Pfizter, Magnetospheric magnetic field modeling, *Annual Scientific Report*, 1977.
- Paulikas, G. A., and J. B. Blake, Effects of the solar wind on magnetospheric dynamics: Energetic electrons at synchronous orbit, in *Quantitative modeling of Magnetospheric Processes*, edited by W. P. Olson, vol. 21 of *Geophys. Monograph*, p. 180, AGU, Washington, D.C., 1979.

Reeves, G. D., R. D. Belian, T. C. Cayton, M. G. Henderson, R. A. Christensen, P. S.

McLachlan, and J. C. Ingraham, Using los alamos geosynchronous energetic particle data in support of other missions, in *Satellite-Ground Based Coordination Source Book*, edited by M. Lockwood, H. J. Opgenoorth, M. N. Wild, and R. Stampe, p. 263, 1997.

Reeves, G. D., D. N. Baker, R. D. Belian, T. E. Cayton, J. F. Fennell, R. H. W. Friedel, M. M. Meier, R. S. Selesnick, and H. E. Spence, The global response of relativistic radiation belt electrons to the January 1997 magnetic cloud, *unknown, unknown, unknown, unknown*.

Roederer, J. G., *Dynamics of Geomagnetically Trapped Radiation*, Springer-Verlag, New York, 1970.

Schulz, M., and L. J. Lanzerotti, *Particle Diffusion in the Radiation Belts*, Springer-Verlag, Berlin, 1974.

Selesnick, R. S., and J. B. Blake, On the source location of radiation belt relativistic electrons, *J. Geophys. Res.*, 1999.

Space-Systems-Loral, ed., *Space Environment Monitor Subsystem*, chap. Space Environment Monitor Subsystem, p. 58, Space-Systems-Loral, 1996.

K. L. McAdams, G. D. Reeves and R. Friedel, Los Alamos National Laboratory,

P.O. Box 1663, MS D466, Los Alamos, NM 87545 (email: kmcadams@nis.lanl.gov, reeves@lanl.gov, and rfriedel@lanl.gov);)

Received _____

Submitted to *Journal of Geophysical Research*, 2000.

This manuscript was prepared with AGU's L^AT_EX macros v5, with the extension package 'AGU⁺⁺' by P. W. Daly, version 1.5d from 1997/04/28.

Table 1.

Table 2.

Figure Captions

Figure 1. Solar wind conditions for the four storms: a) Jan 97; b) May 97; c) Sept 98; and d) Oct 98. The top panel in each stack shows the Dst index (nT). The lower three panels are from the WIND spacecraft and show the z-component of the interplanetary magnetic field (B_Z), the solar wind ion density (n_{sw} , cm^3), and the solar wind velocity (v_{sw}) in km/s, respectively. NEED TO THANK CORRECT PEOPLE HERE

Figure 2. Global relativistic electron mappings. The > 1.5 MeV electron fluxes from the synthesis of eleven satellites for the four GEM storms: a) Jan 97, b) May 97, c) Sept 97, d) Oct 98.

Figure 3. Relativistic electron fluxes from ten satellites at $L = 4.25$ and 6.6 . a) shows the relativistic electron fluxes at $L=4.25$ and 6.6 color coded by satellite. b) May 97, c) Sept 98, d) Oct 98

Figure 4. Spectral evolution of the relativistic electron fluxes for the four storms at $L = 4.25$ (GPS) and $L = 6.6$ (LANL satellites). C and E_o are the coefficients of the spectral fit to a power law: $f(E) = C \exp(-E/E_o)$. a) Jan 97, b) May 97, c) Sept 98, d) Oct 98

Figure 5. Phase space density at constant $/mu$ at $L = 4.25$ (GPS) and $L = 6.6$ (LANL satellites) for different values of $/mu$. In each stack, panels show the PSD for each L-shell at increasing values of $/mu$. The PSD points are color coded for each satellite. a) Jan 97 b) May 97

Figure 6. Similar to Figure 5 except for a) Sept 98 and b) Oct 98

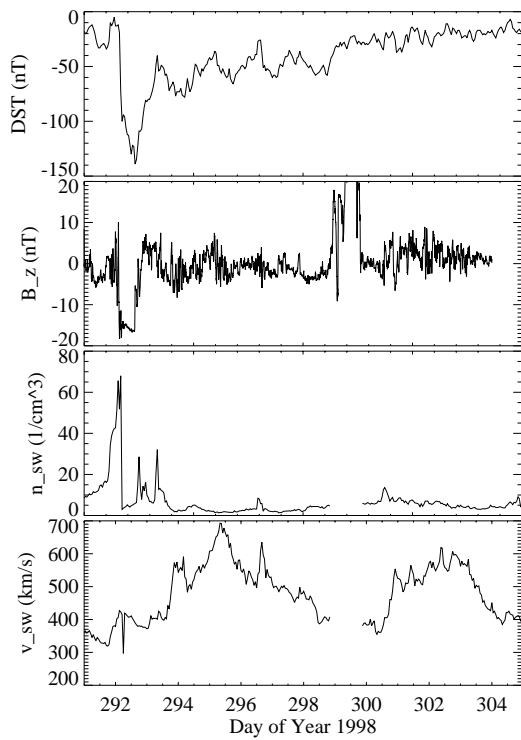
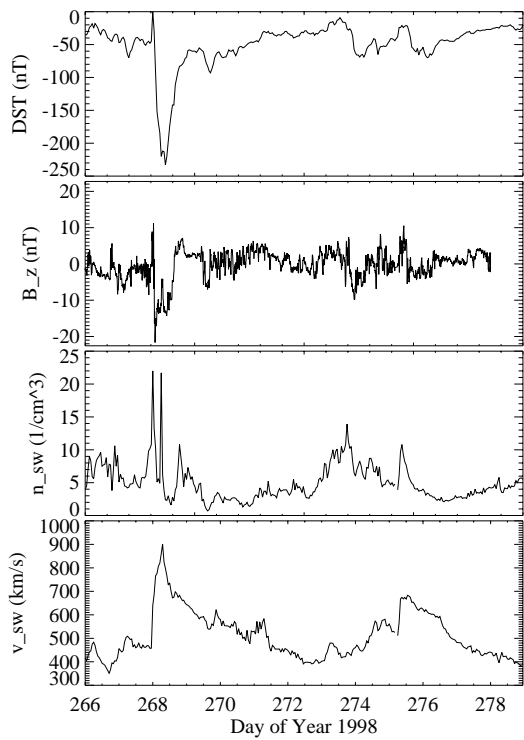
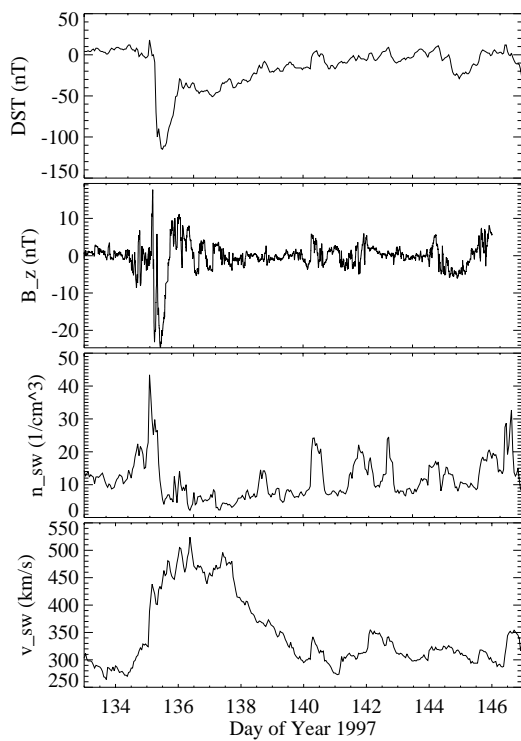
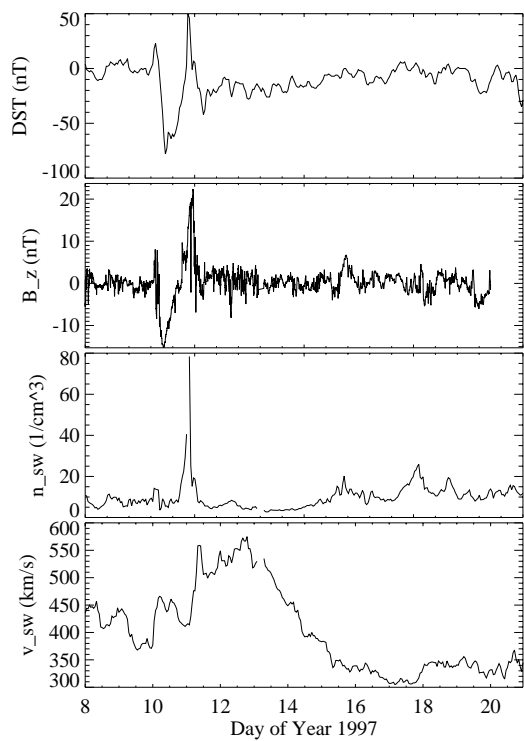
Tables

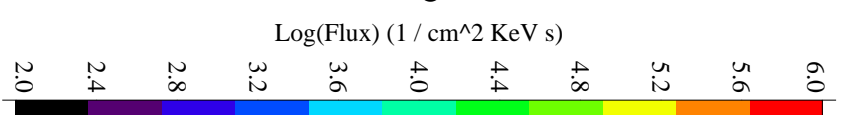
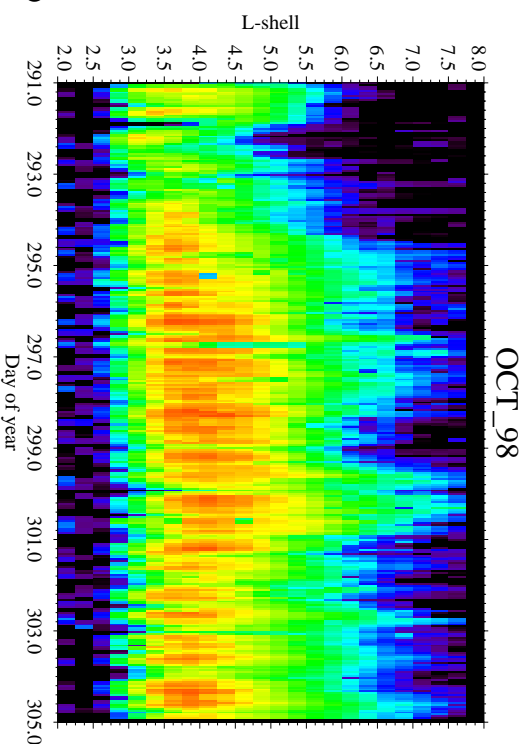
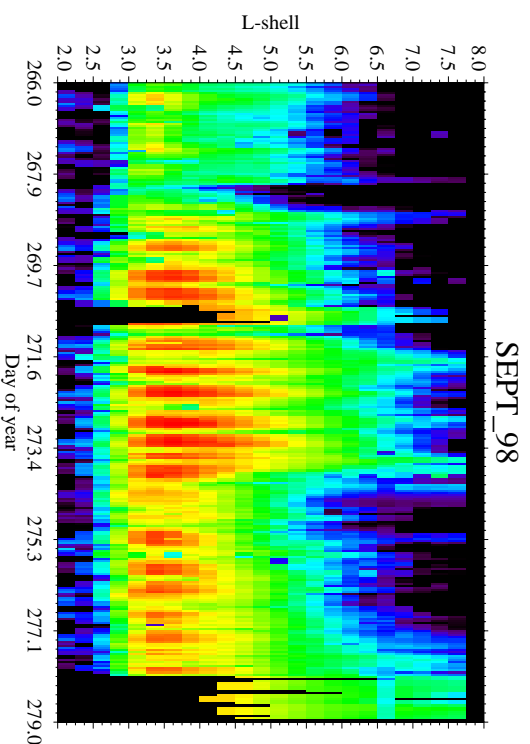
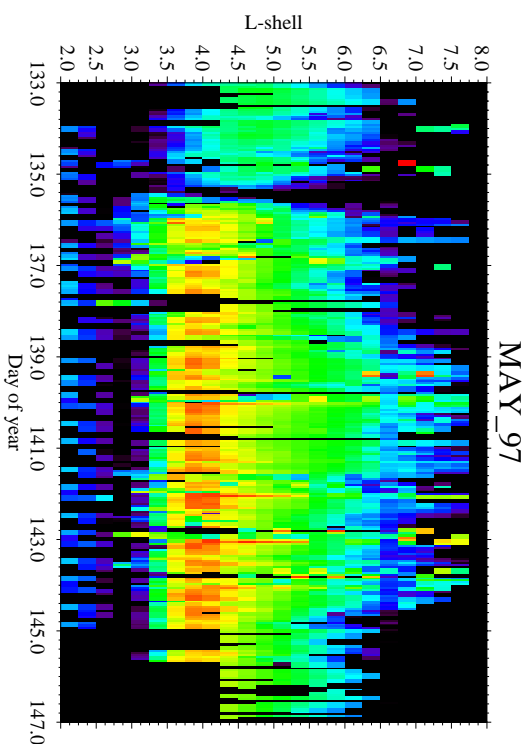
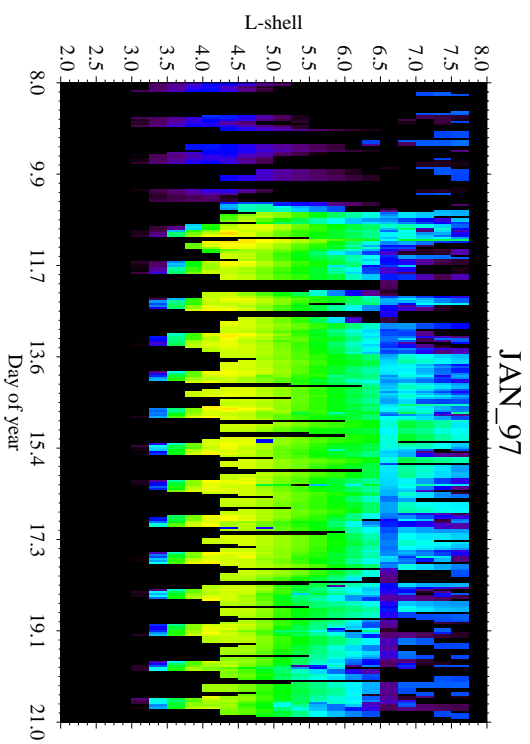
Table 1. Satellite Specification

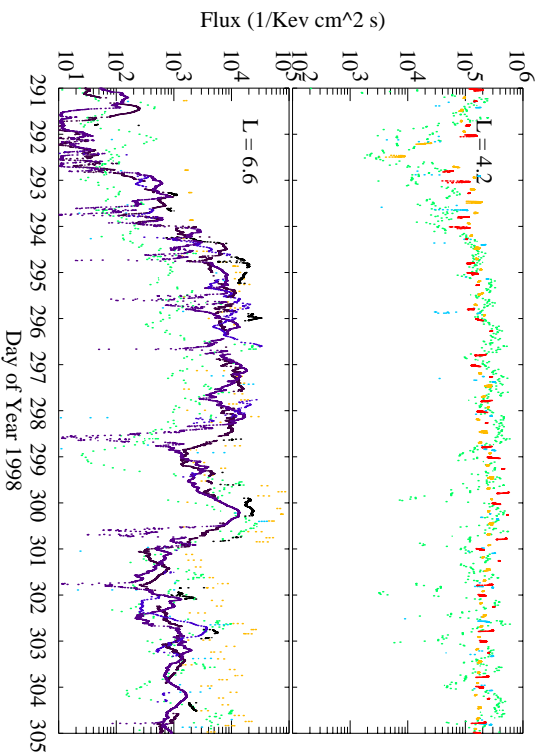
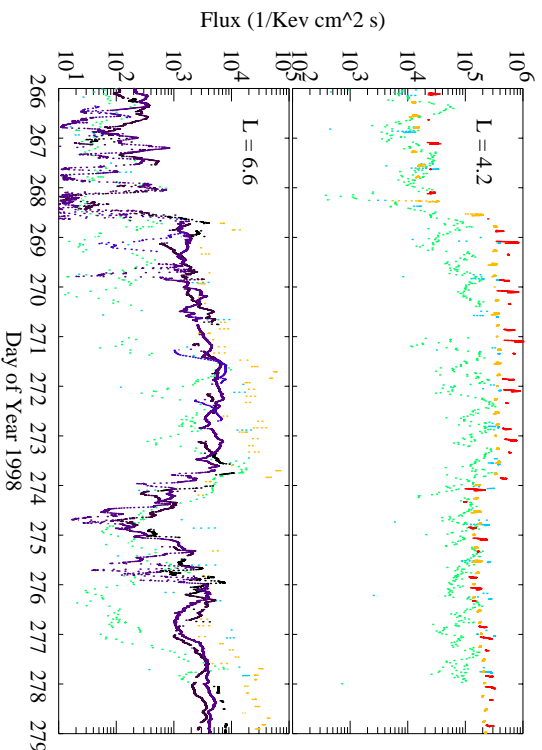
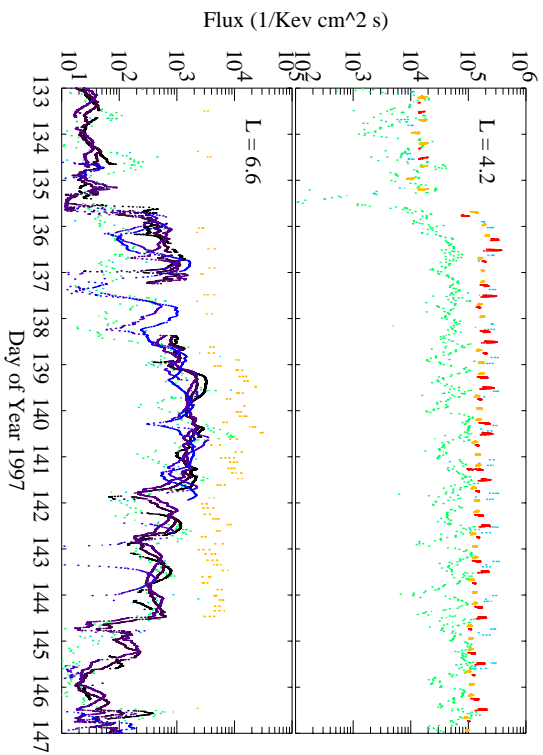
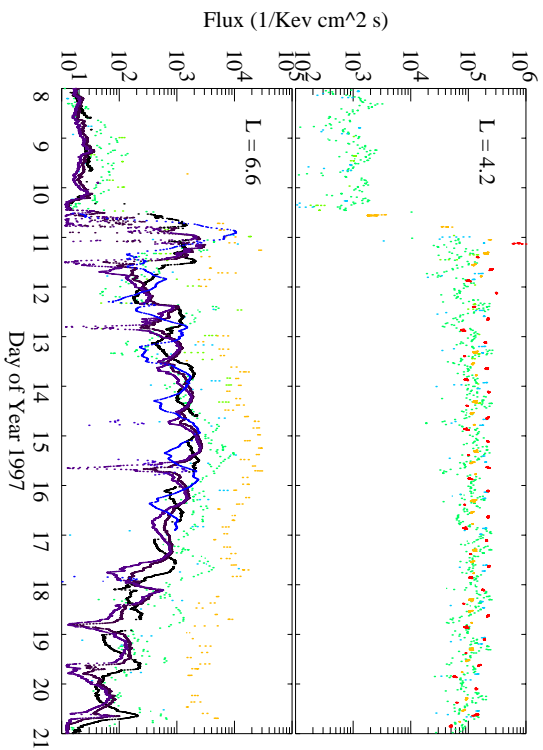
Satellite	Electron energy range (MeV)	Magnetometer	Apogee (R_e)	Orbital Period (hours)
POLAR	$E > 1.4$	yes	8?	18
GOES (8 & 9)	$E > 2$	yes	6.6	24
GPS (24 & 33)	$E > 1.6$	no	4	12
LANL (084, 080, 095)	$E > 1.8$	no	6.6	24
HEO	$E > 1.5$	no	??	12
SAMPEX	$2 < E < 6$	no	2?	1.5

Table 2. Overview of GEM storms

	Jan 97	May 97	Sept 98	Oct 98
Dst Minimum (nT)	-85	-170	-228	-140
Kp Maximum	6.0	6.0	8.0	6.0
Solar Wind Density (cm^{-3})	200	44	20	66
Solar Wind Velocity (km/s)	600	500	930	680
Ion pressure (SW) (nPa)	53	17	24	25
Peak Flux at L = 4.4	1×10^5	2×10^5	4×10^5	3×10^5
Peak Flux at L = 6.6	3×10^3	3×10^3	7×10^3	2×10^4
ULF Wave Power				
Polar Cap Index	NA	40	100	45







1990-095

1990-095

1990-095

GOES_8

GOES_9

POLAR

SAMPEX

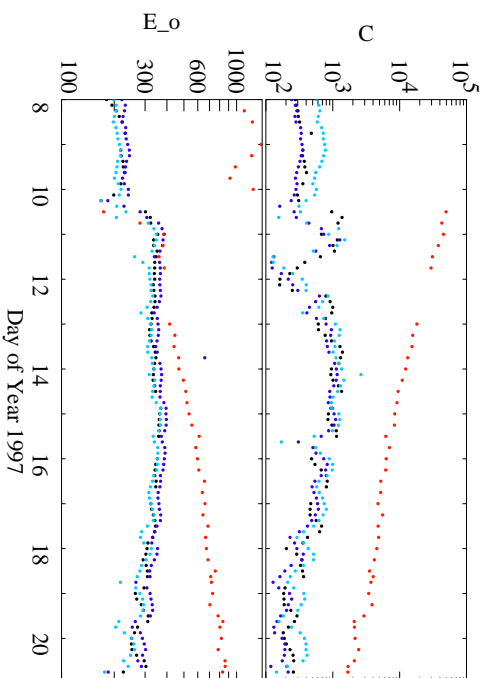
HEO

GPS 33

GPS 24

1990-095

1991-080



1994-084

GPS 33

